RESEARCH ARTICLE

NANO · MICRO small
www.small-journal.com

Unlocking the Potential of Iron Sulfides for Sodium-Ion Batteries by Ultrafine Pulverization

Hui Wu, Guanglin Xia, and Xuebin Yu**

Iron sulfides have attracted tremendous research interest for the anode of sodium-ion batteries due to their high capacity and abundant resource. However, the intrinsic pulverization and aggregation of iron sulfide electrodes induced by the conversion reaction during cycling are considered destructive and undesirable, which often impedes their capacity, rate capability, and long-term cycling stability. Herein, an interesting pulverization phenomenon of ultrathin carbon-coated $Fe_{1-x}S$ nanoplates ($Fe_{1-x}S$@C) is observed during the first discharge process of sodium-ion batteries, which leads to the formation of $Fe_{1-x}S$ nanoparticles with quantum size (≈5 nm) tightly embedded in the carbon matrix. Surprisingly, no discernible aggregation phenomenon can be detected in subsequent cycles. In/ex situ experiments and theoretical calculations demonstrate that ultrafine pulverization can confer several advantages, including sustaining reversible conversion reactions, reducing the adsorption energies, and diffusion energy barriers of sodium atoms, and preventing the aggregation of $Fe_{1-x}S$ particles by strengthening the adsorption between pulverized $Fe_{1-x}S$ nanoparticles and carbon. As a result, benefiting from the unique ultrafine pulverization, the $Fe_{1-x}S$@C anode simultaneously exhibits high reversible capacity (610 mAh g^{-1} at 0.5 A g^{-1}), superior rate capability (427.9 mAh g^{-1} at 20 A g^{-1}), and ultralong cycling stability (377.9 mAh g^{-1} after 2500 cycles at 20 A g^{-1}).

1. Introduction

Sodium-ion batteries (SIBs) have recently emerged as an economically promising alternative to conventional lithium-ion batteries (LIBs) owing to the cheap price and abundant natural distribution of Na resources.[1,2] Although SIBs work on similar electrochemical mechanisms to LIBs, the development of SIBs falls far behind that of LIBs due to the intrinsic larger ion radius of Na^+ than that of Li^+, leading to poor cycling stability and unsatisfying rate performance.[3] In addition, the higher negative redox potential of Na compared with that of Li makes it much more difficult to find desirable electrode materials for SIBs. Therefore, developing and preparing suitable anode materials of SIBs with high performance for practical applications is highly desirable, yet challenging.

Transition-metal sulfides (TMSs) (e.g., $Fe_{1-x}S$,[4,5] FeS_2,[6,7] MoS_2,[8,9] Ni_3S_2,[10,11] Sb_2S_3,[12,13] and CoS)[14,15] have been intensively investigated as anode materials of SIBs because of their pronouncedly high theoretical capacities based on conversion reaction or even alloy reaction mechanism.[4,16] Among them, iron sulfides have attracted increasing attention as anodes for SIBs due to the high sodium storage capacity (e.g., 610 mAh g^{-1} for $Fe_{1-x}S$), high voltage plateaus, low cost, high abundance, and eco-friendliness.[17] It has been demonstrated that iron sulfides undergo an intercalation-to-conversion reaction sequence upon sodiation during the initial discharge cycle.[18] However, the sodiation/desodiation process is inevitably accompanied by serious volume variations caused by the conversion reaction, which leads to the severe destruction of the electrode structure and hence rapid capacity loss and deteriorative cycle lifetime.[19] To solve this problem, Chen et al. adjusted the discharge cut-off voltage to 0.8 V to avoid the huge volume variations caused by the conversion reaction, in which only the interaction reaction happened during the discharge and charge processes. To mitigate the significant volume variations resulting from the conversion reaction, Chen et al. opted to adjust the discharge cut-off voltage to 0.8 V, allowing only the interaction reaction to occur during both the discharge and charge processes.[20] As a result, the FeS_2 electrode offered unprecedented long-term cyclability with a capacity retention of ≈90% over 20 000 cycles. However, this cut-off voltage modulation strategy leads to an inevitable capacity loss due to the lack of a complete conversion reaction, which predominantly contributes to the overall capacity of the intercalation-to-conversion reaction. Moreover, the iron sulfide-based anodes also face the issues of poor electrical conductivity and sluggish Na^+ ion diffusion kinetics.[19,21] Owing to the sluggish reaction kinetics in iron sulfide electrode materials, the irreversible surface-limited redox reaction always occurs in bulk electrode materials, thus impeding successive conversion cycles.[22] It can lead to incomplete conversion reactions and will repeat the reaction in subsequent cycling, resulting in forming a thick insulating layer, and

H. Wu, G. Xia, X. Yu
Department of Materials Science
Fudan University
Shanghai 200433, China
E-mail: xiaguanglin@fudan.edu.cn; yuxuebin@fudan.edu.cn

The ORCID identification number(s) for the author(s) of this article can be found under https://doi.org/10.1002/smll.202312190

DOI: 10.1002/smll.202312190

thus leading to serious capacity decay.[23] To address these problems, some feasible solutions have been proposed including morphology modification, atomic-level engineering, and iron sulfide composites.[24] Among them, reducing the size of electrode material to nanoscale combined with the carbon modification has been identified as one of most effective and promising electrode configurations, which could not only enhance electrical conductivity of the whole electrode, but also improve the reaction kinetics of the active materials, as well as alleviate structural degradation during the conversion reaction.[25] Unfortunately, even though these strategies are effective to improve the electrochemical performance to a certain extent, the fabrication of iron sulfide anodes simultaneously delivering large capacity, fast charging capability, and high cyclability is still a challenge, which is related to the evitable pulverization problems induced by volume expansion and incomplete conversion reaction during repeated sodiation and desodiation process.

Recently, some reports demonstrated that the iron sulfide nanoparticles with quantum size (d<10 nm) could overcome the kinetic and thermodynamic limitations of the Na—S conversion reaction, realizing the highly reversible, and efficient conversion reaction to offer higher specific capacity.[26,27] The quantum size comparable to or smaller than the diffusion lengths of Fe ($L_D \approx 10^{-18}$ cm^2 s^{-1} at room temperature) in iron sulfides can yield thermodynamically reversible nanodomains of converted Fe^0 metal and Na_xS conversion products during cation exchange.[26] Considering the short diffusion distances of Fe, the desired particle size of iron sulfides <10 nm could enable a relatively complete conversion reaction. For example, Choi et al. designed Fe_7S_8 nanoparticles with an average size of 10 nm encapsulated in carbon, which delivered a high rate capacity (550 mAh g^{-1} at 2.7 A g^{-1}) and superior high and stable capacity (447 mAh g^{-1} at 0.18 A g^{-1} after 1000 cycles) in SIBs.[26] Given the above analysis, it is highly expected to realize high-performance iron sulfide anodes by combining the ultrafine iron sulfides particles with quantum size and conductive carbonaceous materials to achieve high reversible capacity, excellent rate capability, and superior long-term cyclability in SIBs simultaneously.

In this work, we designed and synthesized ultrathin carbon-coated $Fe_{1-x}S$ ($Fe_{1-x}S$@C) nanoplates by a facile coating-carbonation-sulfidation strategy. The size of the $Fe_{1-x}S$@C nanoplates with a carbon layer could be reduced to ≈ 5 nm. When evaluated as an anode for SIBs, an ultrafine pulverization phenomenon of the $Fe_{1-x}S$@C electrode was unexpectedly observed during the initial discharge cycle. Impressively, instead of suffering from serious capacity fading, the pulverized $Fe_{1-x}S$@C electrode simultaneously exhibited high capacity, superior rate capability, and ultralong cycling lifetime. Ex situ HRTEM analysis revealed that the $Fe_{1-x}S$@C nanoplates were pulverized into small particles with quantum size (≈5 nm) and tightly embedded in the carbon matrix. More impressively, there was no discernible aggregation phenomenon was detected in subsequent cycles. In situ XRD and Raman demonstrated that the pulverized nanoparticles could overcome the significant kinetic and thermodynamic limitations of the conversion reaction, realizing the highly reversible conversion reaction of $Fe_{1-x}S$. Moreover, Density functional theory (DFT) calculations further deciphered that this ultrafine pulverization of carbon-coated $Fe_{1-x}S$ nanoplates could not only significantly reduce both the adsorbed energies and diffusion energy barriers of Na atom but also effectively prevent the aggregation of $Fe_{1-x}S$ particles by strengthening the adsorption between pulverized $Fe_{1-x}S$ nanoparticles and carbon. As a result, benefiting from the unique ultrafine pulverization, the $Fe_{1-x}S$@C anode exhibited a high reversible capacity of 610 mAh g^{-1} at 0.5 A g^{-1}, superb rate capability of 427.9 mAh g^{-1} at 20 A g^{-1}, and ultralong cycling stability over 2500 cycles at 20 A g^{-1}. This work holds a meaningful insight into the pulverization phenomenon in electrode study.

2. Results and Discussion

Figure 1a schematically illustrates the fabrication process of the $Fe_{1-x}S$@C nanoplates. that involves polydopamine coating, carbonization, and sulfidation treatment. The phase of FeOOH, intermediate products (Fe_3O_4@C), and $Fe_{1-x}S$@C was characterized by X-ray diffraction (XRD) patterns (Figure S1, Supporting Information). The XRD patterns of $Fe_{1-x}S$@C samples (Figure S1c, Supporting Information) showed all the diffraction peaks, which could be indexed to $Fe_{1-x}S$ (Card No. 29–0726). The TEM images of FeOOH and Fe_3O_4@C were displayed in Figure S2 (Supporting Information), and both of them were plate-like nanoparticles. The resulting samples at sulfidation temperatures of 400 and 500 °C were detonated as $Fe_{1-x}S$@C-400 and $Fe_{1-x}S$@C-500, respectively. Figure 1b displays the transmission electron microscopy (TEM) image of $Fe_{1-x}S$@C-400 nanoplates and the selected area electron diffraction (SAED) pattern of $Fe_{1-x}S$@C nanoplate (the insert in Figure 1b). It can be seen that the plate-like structure was well preserved after sulfidation. Besides, the TEM image of $Fe_{1-x}S$@C-500 nanoplates was recorded in Figure S3 (Supporting Information), and its morphology exhibited little structural distortion compared with that of $Fe_{1-x}S$@C-400 nanoplates. Figure 1c,d showed the high-angle annular dark-field scanning transmission electron microscopy (HAADF-STEM) images of the as-prepared $Fe_{1-x}S$@C-400, and it showed the porous nanoplates with a thickness of ≈5.1 nm and an inplane extension as long as 50–250 nm. Besides, the high-resolution transmission electron microscopy (HRTEM) exhibited that the thickness of the carbon layer was ≈2.7 nm, and a characteristic interplanar distance of 0.263 nm was consistent with the inter-plane distance of $Fe_{1-x}S$ (2011) plane[28] (Figure 1e,f). The STEM energy-dispersive spectroscopy (EDS) mapping images revealed the existence of an N-doped carbon layer and the homogenous distribution of N, C, S, and Fe elements in the composite (Figure 1g,g_{1-5}). The N_2 adsorption–desorption measurements revealed that $Fe_{1-x}S$@C composites had large Brunauer–Emmett–Teller (BET) specific surface areas. The surface area of $Fe_{1-x}S$@C composites increased from 85.4 to 116.6 m^2 g^{-1} for $Fe_{1-x}S$@C-500 and $Fe_{1-x}S$@C-400, respectively, as displayed in Figure S4 (Supporting Information). Furthermore, X-ray photoelectron spectroscopy (XPS) was carried out to characterize the surface chemical composition of the $Fe_{1-x}S$@C composite. The existence of C, Fe, and S elements was confirmed in the survey spectrum (Figure S5a, Supporting Information). The high-resolution C 1s XPS spectrum in Figure S5b (Supporting Information) could be deconvoluted into three peaks at 284.6, 286.2, and 288.7 eV, which were attributed to the C—C, C—O, and O—C=O, respectively.[29] In the Fe 2p XPS spectrum (Figure S5c,

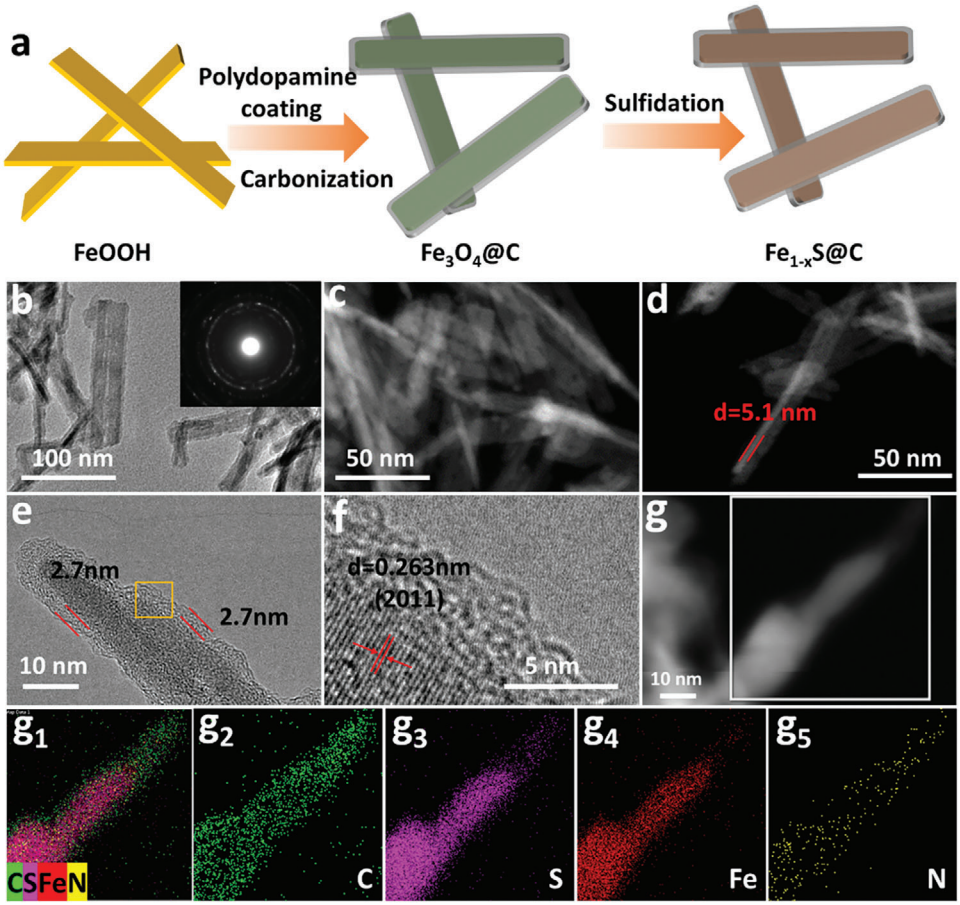

Figure 1. Schematic illustration of the synthetic process for $Fe_{1-x}S$@C nanoplates and microstructure characterization of $Fe_{1-x}S$@C-400. a) Schematic illustration of the preparation process of the $Fe_{1-x}S$@C nanoplates. b,f,g) TEM image of $Fe_{1-x}S$@C-400. c and d) STEM image of $Fe_{1-x}S$@C-400 composite. f) FESEM image and e,f) TEM image of $Fe_{1-x}S$@C-400 composite. g and g_{1-5}) STEM-EDS mapping images of $Fe_{1-x}S$@C-400 composite.

Supporting Information), two peaks located at 711.9 and 726.2 eV were observed, which were ascribed to the Fe $2p_{1/2}$ and Fe $2p_{3/2}$, respectively. As seen from the S 2p XPS spectrum in Figure S5d (Supporting Information), the peak at 167.9 eV could be assigned to SO_x due to the surface oxidation, and peaks at 164.2 and 163.1 eV are related to the S $2p_{1/2}$ and S $2p_{3/2}$ in the $Fe_{1-x}S$, respectively. A C—S peak appeared at ≈163.5 eV, demonstrating the chemical bonding between the carbon shell and the $Fe_{1-x}S$ core shell.[30] In Raman spectra (Figure S6, Supporting Information), the two peaks at 1354 and 1588 cm^{-1} could be assigned to the D and G bands of carbon materials, respectively.[31] The I_D/I_G ratios of $Fe_{1-x}S$@C-400 and $Fe_{1-x}S$@C-500 were 0.93 and 0.89, respectively, indicating a low graphitization of the carbon layer.

The electrochemical performances of $Fe_{1-x}S$@C composites as SIBs anodes were tested, and the results were presented in **Figure 2**. Figure 2a shows cyclic voltammetry (CV) curves of the $Fe_{1-x}S$@C-400 electrode for the first three cycles in a potential window of 0.01–3 V at 0.1 mV s^{-1}. In the 1st cathodic scan, a weak reduction peak at ≈1.56 V could be associated with the sodiation process of generation of the Na-rich phase ($Na_yFe_{1-x}S$).[21] A weak peak at 1.2 V, a sharp cathodic peak at 0.9 V, and a broad peak at 0.64 could be assigned to the reaction of Na and $Na_yFe_{1-x}S$ accompanied by the formation of Fe, Na_2S, and Na-rich phases depending on the quantity of Na transfer.[32] Notably, these three peaks also involved the contribution from the decomposition of electrolyte and formation process of solid electrolyte interface (SEI) film because their intensities exhibited remarkable decay in the next cycles.[5] Besides, a broad peak centered at 0.32 V could be attributed to the conversion reaction to form Fe and Na_2S.[33] Additionally, the clear cathodic peak ≈0.04 V was ascribed to Na^+ insertion into carbon. During the first anodic scan, a sharp peak at 0.073 V was attributed to the Na^+ extraction from carbon materials, which was similar to the previous works.[34,35] Besides, three anodic peaks centered at 1.35, 1.53, and 1.81 V might be related to the reverse conversion reaction between metallic Fe and Na_2S matrix with the formation of Na_2FeS_2.[36–38] In addition, two broad peaks at ≈2.1 and 2.6 V could be ascribed to the multiple-step Na^+ desodiation from Na_2FeS_2 with the generation of $Na_{2-n}FeS_2$ and FeS_x.[39] From the second cycle onward, there was no obvious loss of peak area in the successive cycles, indicating the highly reversible electrochemical reaction in the $Fe_{1-x}S$ composite after the first sodiation/desodiation process. Besides, CV curves of $Fe_{1-x}S$@C-500 were also recorded, showing a similar profile to that of $Fe_{1-x}S$@C-400 (Figure S7, Supporting Information). The charge/discharge profiles of $Fe_{1-x}S$@C from the 1st to 10th cycle at 0. 5 A g^{-1} was displayed in Figure 2b.

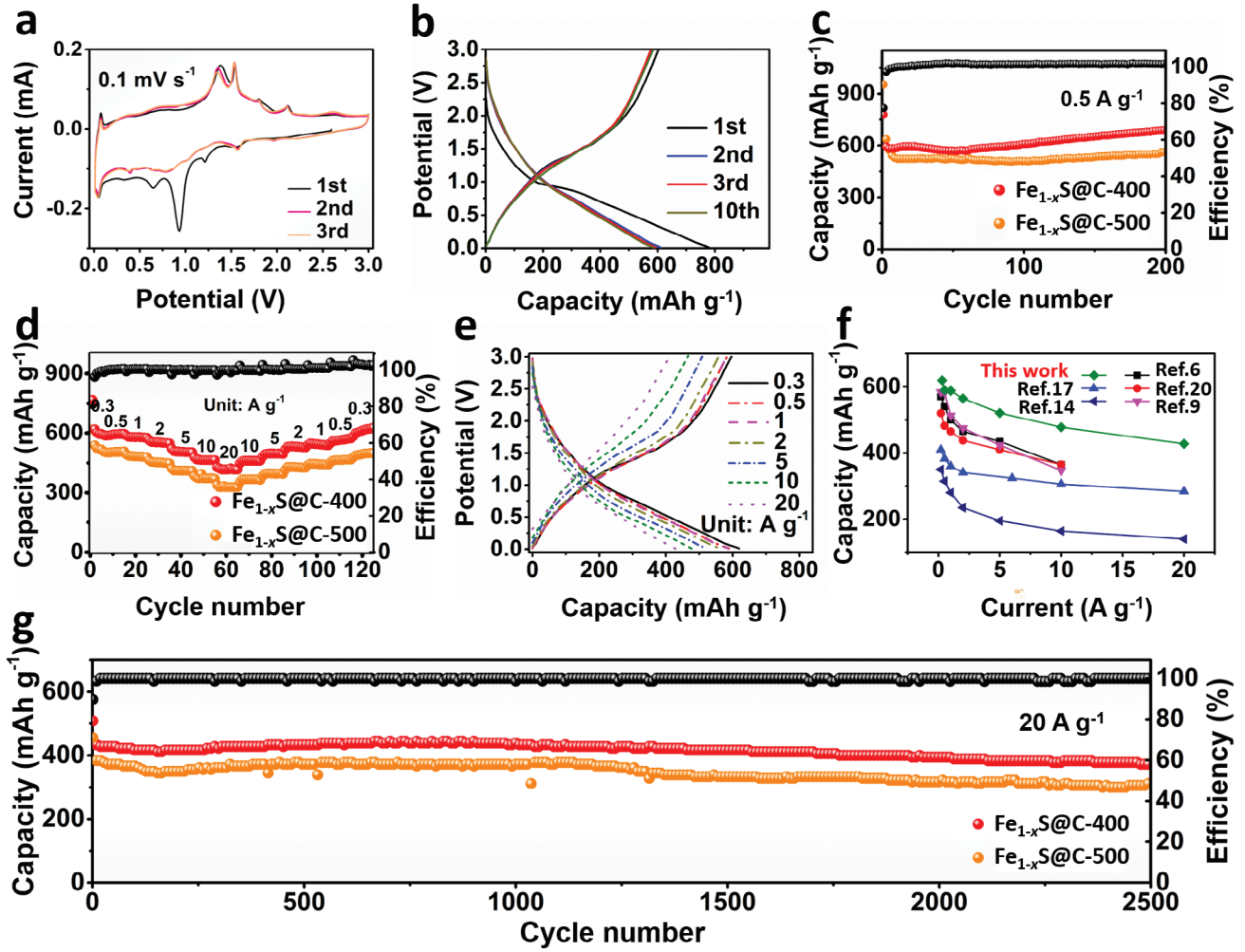

Figure 2. Sodium storage performance of $Fe_{1-x}S$@C composites. a) CV curves of $Fe_{1-x}S$@C nanoplates at 0.1 mV s^{-1}. b) Charge–discharge profiles of $Fe_{1-x}S$@C at different cycles (from selected cycles as indicted); c) Cycle performance of $Fe_{1-x}S$@C composites at 0.5 A g^{-1}; d) Rate performance of $Fe_{1-x}S$@C composites; e) Charge–discharge profiles of $Fe_{1-x}S$@C at different current densities; f) Comparison of rate performance between $Fe_{1-x}S$@C-400 and as-reported iron sulfide anodes for SIBs; g) Long-term cycling performance of $Fe_{1-x}S$@C composites at 20 A g^{-1}.

They were almost overlapped, suggesting a stable electrochemical reversibility of the $Fe_{1-x}S$@C electrode after the initial discharge process. Figure 2c exhibits the cyclic performance of as-prepared $Fe_{1-x}S$@C composites. The initial charge/discharge capacity of $Fe_{1-x}S$@C-400 anode was 610.5 and 779 mAh g^{-1}, respectively, with a Coulombic efficiency (CE) of 77.5%. The capacity loss was primarily attributed to the irreversible formation of the SEI films. The CE rapidly increased to ≈95.4% in the second cycle and could be maintained at a high level of >98% in the following cycles. The $Fe_{1-x}S$@C-400 anode delivered a reversible capacity of 690.2 mAh g^{-1} after 200 cycles, respectively, which was higher than that of the $Fe_{1-x}S$@C-500 anode (560 mAh g^{-1} after 200 cycles). Moreover, the rate capabilities of both anode materials were also studied at a sequence of current densities from 0.3 to 20 A g^{-1}, and further sequentially decreased to 0.3 A g^{-1}. As displayed in Figure 2d, the $Fe_{1-x}S$@C-500 delivered discharge capacities of 523.4, 503.1, 484.8, 453.2, 411.3, 372.1, and 327.2 mAh g^{-1} at specific currents of 0.3, 0.5, 1, 2, 5, 10, and 20 A g^{-1}, respectively. When tested at the same current densities, the rate capacities of the $Fe_{1-x}S$@C-400 sample were 619.2, 589.8, 587.8, 564.6, 520.9, 477.9, and 427.9 mAh g^{-1}, respectively. Upon returning the current density to 0.3 A g^{-1}, the $Fe_{1-x}S$@C-400 sample still delivered a discharge capacity of ≈626.4 mAh g^{-1}, slightly higher than the initial discharge capacity, indicating stable SEI formation and reduced the dissolution of polysulfide during the rate capability test.[40] Comparatively, the $Fe_{1-x}S$@C-500 electrode delivered a relatively low rate capacity, which could be mainly attributed to slower charge transfer kinetics, as discussed later. The discharge/charge profiles at different rates were shown in Figure 2e. The flat section sharply decreased at stepwise current densities, indicating that the adsorption of Na ions at the active site became much faster. In other words, the pulverization of active materials could shorten the diffusion distance of Na ions and improve the diffusion rate. The sufficient active sites could enhance the sodium storage capacity by capturing more Na ions and improving surface-controlled pseudocapacitive effect. To assess the rate and long-term cycle performance of our $Fe_{1-x}S$ composites, previously reported iron sulfide anodes were examined for

comparison, as shown in Figure 2f and Figure S8 (Supporting Information). The long-term cycling performance of the $Fe_{1-x}S$@C samples was further evaluated at a large current density of 20 A g^{-1}, as displayed in Figure 2g. All of them exhibited excellent cycle life up to 2500 cycles without obvious capacity fading. The reversible capacity of $Fe_{1-x}S$@C-400 reached 455.9 mAh g^{-1} in the first cycle and was stabilized at 377.9 mAh g^{-1} after 2500 cycles with a capacity retention of 82.8%, which was significantly higher than that of $Fe_{1-x}S$@C-500 (305.7 mAh g^{-1} after 2500 cycles with a capacity retention of 76.4%).

To further visually illustrate the phase transition, microstructure, and morphology evolution during the sodiation/desodiation process, ex situ TEM was carried out to monitor the cycling process of $Fe_{1-x}S$@C-400. TEM, HRTEM, SAED pattern, and STEM-EDS mapping images of $Fe_{1-x}S$@C-400 electrode at first discharged state (0.01 V) and charged state (3.0 V) in the cut-off range of 0.01–3.0 V were presented in **Figure 3**. Unexpectedly, the ultrafine pulverization of $Fe_{1-x}S$@C nanoplates happened after the first discharge cycle. It could be seen that the $Fe_{1-x}S$@C nanoplates disappeared and pulverized into ultrafine nanoparticles with quantum size (≈5 nm), as shown in Figure 3a,b. Additionally, the obvious d-spacings of 0.308 and 0.201 nm in Figure 3c could be assigned to the (200) plane of Na_2S and (110) plane of Fe, respectively. The corresponding SAED pattern was well indexed to the diffraction patterns of the Na_2S and Fe phases (Figure 3d), suggesting a deep conversion reaction. The STEM-EDS mapping images in Figure 3e indicate the existence of Fe and S elements, verifying a significant pulverization phenomenon. When charging the cell back to 3.0 V, the TEM images (Figure 3f,g) reveal that aggregation of the ultrafine nanoparticles had not taken place. Noticed that there were no discernable changes in the size and morphology of charged product compared to that of the initial discharge product. Figure 3h shows the d-spacings of 0.213 and 0.272 nm, which matched well with the (2022) and (2011) planes of $Fe_{1-x}S$, respectively, which demonstrated that the formation of $Fe_{1-x}S$ and the high reversibility of the electrode. Besides, the corresponding SAED pattern was well indexed to the diffraction patterns of the $Fe_{1-x}S$ phase (Figure 3i). The STEM-EDS mapping images suggested that the Fe and S elements of the $Fe_{1-x}S$ phase composite were uniformly distributed in the carbon matrix (Figure S9, Supporting Information). To check the state of active material particles in the subsequent cycles, TEM images of the electrodes at full charge state after 100 and 200 cycles were recorded in Figure 3j–m, respectively. There was no discernable aggregation observed, indicating the superior stability of the $Fe_{1-x}S$ electrode after ultrafine pulverization. In addition, a similar pulverization phenomenon was also observed in the $Fe_{1-x}S$@C-500 anode after full discharge, as displayed in Figure S10 (Supporting Information). The average sizes of the pulverized particles were ≈9 nm, which was a little larger than that of the $Fe_{1-x}S$@C-400 anode, which could be related to the different degree of crystallinity, graphitization of carbon layer, and structural distortion resulting from higher temperature calcination. As revealed from the above analysis, the $Fe_{1-x}S$@C composite after pulverization remained granular without aggregation during the subsequent discharge–charge process. that could be the primary reason for the outstanding sodium storage performance. The schematic illustration of the particle pulverization processes was summarized in Figure 3n. We have observed that the reaction mechanism involved differs from the common ones. Typically, the pulverization of electrode materials often leads to material aggregation and subsequent capacity decay. In the case of this particular phenomenon, the paper will provide further insights through theoretical calculations. Additionally, it is noteworthy that the generation of $Fe_{1-x}S$ is observed after complete charging, which deviates from previous studies and suggests an incomplete reversibility. This further confirms that the pulverization of quantum dots can be attributed to a nanoparticle size comparable to or smaller than the diffusion length of Fe during cation exchange, resulting in thermodynamically reversible nanodomains of converted Fe metal, and Na_2S conversion products.

To further reveal the voltage-dependent phase transformation behavior of $Fe_{1-x}S$@−400 during the first discharge/charge process, in situ XRD was carried out and the results were presented in **Figure** 4a,b. It was noted that the two peaks located at 38.5° and 34.7° were ascribed to aluminum foil and Be, respectively.[17,41] Apparently, the intensity of all the diffraction peaks of $Fe_{1-x}S$@C-400 visibly decreased during the discharge process. According to in situ XRD data, a four-stage process combined with insertion/conversion mechanisms was concluded, which agreed with previous reports.[37,42] The reaction processes during the first sodiation/desodiation process were depicted with color-coding for overall understanding. In the first stage, the peaks at 29.5° and 33.6° belonged to the (200) and (2011) facets of $Fe_{1-x}S$, respectively, exhibiting a slight shift to a lower angle when it discharged from OCV to ≈0.8 V.[32,43] This phenomenon could be assigned to the insertion of sodium ions into $Fe_{1-x}S$ and the formation of $Na_yFe_{1-x}S$, which led to the increase in interplanar distances. In the second stage, the $Na_yFe_{1-x}S$ was eventually converted to metallic Fe and Na_2S, and the peak intensities of (200) and (2011) gradually weakened and disappeared when it was discharged to 0.01 V. In the third stage, a new peak appeared at 30.8° when it was recharged to ≈0.8 V, which could be attributed to the (221) planes of $NaFeS_2$, indicating the formation of the Na-rich phase (Na_xFeS_y).[44] In the fourth stage, when it charged to 3 V, the XRD patterns could be ascribed to the formation of $Na_{2-n}FeS_2$ and $Fe_{1-x}S$. and the weak intensities of diffraction peaks could be attributed to the ultrafine pulverization phenomenon that led to a reduction in the size of the electrode material and the degree of crystallinity. The related multi-steps sodiation–desodiation reaction mechanism can be described as the following equations:

1) Stage I (intercalation)

$$Fe1-xS + yNa+ + ye- \rightarrow NayFe1-xS \quad (1)$$

2) Stage II (conversion)

$$NayFe1-xS + (2-y)Na+ + 2e- \rightarrow Na2S + (1-x)\,Fe \quad (2)$$

3) Stage III (deconversion)

$$2Na2S + Fe \rightarrow Na2FeS2 + 4Na+ + 4e- \quad (3)$$

4) Stage IV (deintercalation)

$$Na2FeS2 \rightarrow Na2-nFeS2 + nNa+ + 4e- \quad (4)$$

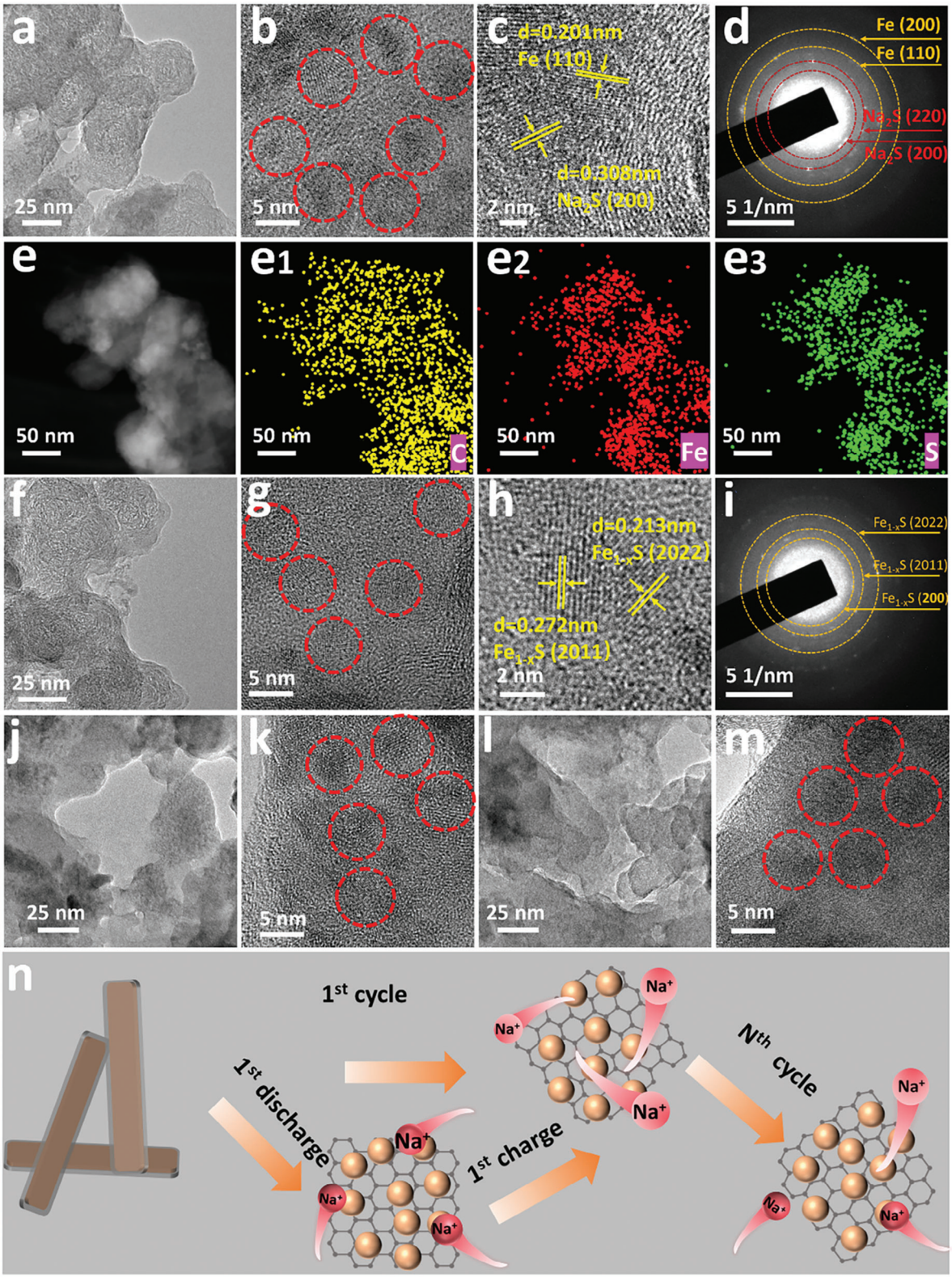

Figure 3. Microstructure characterization of $Fe_{1-x}S$@C-400 electrode during cycling and schematic representation of cycling-dependent evolution of the microstructure of $Fe_{1-x}S$@C-400 electrode; a–e) TEM, HRTEM, SAED pattern, and STEM-EDS mapping images of the $Fe_{1-x}S$@C-400 electrode at fully discharged state (0.01 V); f–i) TEM, HRTEM, HRTEM, and SAED pattern of the $Fe_{1-x}S$@C-400 electrode at fully charged state (3 V); j,k) TEM and HRTEM images of $Fe_{1-x}S$@C-400 electrode after 100 cycles; l,m) TEM and HRTEM images of $Fe_{1-x}S$@C-400 electrode after 200 cycles; n) Schematic illustration of the particle pulverization processes.

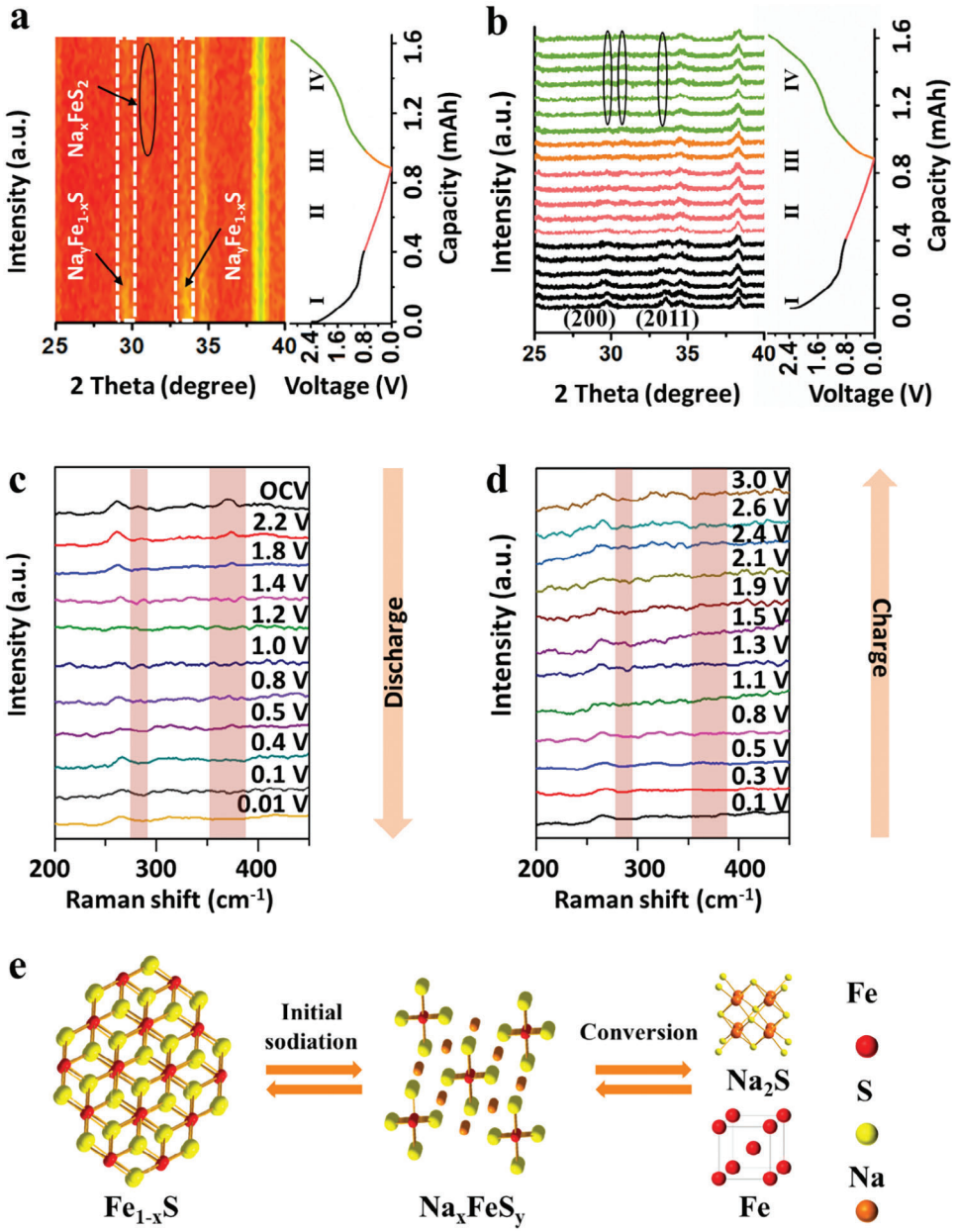

Figure 4. In situ XRD and Raman analysis of $Fe_{1-x}S$@C-400 electrode and reaction mechanism. a) Contour plots of in situ XRD results of $Fe_{1-x}S$@C-400 electrode against the voltage profile during the initial cycle at a cutoff voltage of 0.01–3.0 V; b) Corresponding in situ XRD patterns of $Fe_{1-x}S$@C-400 electrode and corresponding initial discharge and charge profiles of $Fe_{1-x}S$@C-400 electrode; c,d) Stacked in situ Raman patterns of $Fe_{1-x}S$@C-400 electrode during the initial discharge–charge process at different voltages; e) Schematic illustration for the Na storage mechanism of $Fe_{1-x}S$ during the initial discharge–charge process.

$$Na2 - nFeS2 + (1 - 2x)\,Fe \rightarrow 2Fe1 - xS + (2 - n)Na + + e- \quad (5)$$

Furthermore, the Na-storage processes in $Fe_{1-x}S$@C-400 were further investigated by in situ Raman spectroscopy during the initial discharge–charge process, as presented in Figure 4c,d. At the OCV≈2.5 V, the two peaks at ≈287 and 370 cm^{-1} had been reported as characteristic bands of $Fe_{1-x}S$, which are consistent with the symmetric stretching vibrations of Fe—S and the longitudinal optical phonon vibration, respectively.[45,46] The intensity of the peaks gradually decreased during the sodiation process.[47] When the cell was discharged to 0.01 V for complete breaking, the Fe—S peak disappeared, indicating that $Fe_{1-x}S$ reacted with Na and converted into Fe and Na_2S. when recharged back to 3.0 V, two weak broad peaks appeared again at ≈290 and 373 cm^{-1}, indicating the formation of $Fe_{1-x}S$, which was consistent with that of in situ XRD data. The formation of $Fe_{1-x}S$ after fully charged indicated that the ultrafine pulverization of the $Fe_{1-x}S$@C composite overcame the significant kinetic and thermodynamic constraints of electrochemical conversion reactions.[18] This remarkable result can be attributed to the size of pulverized

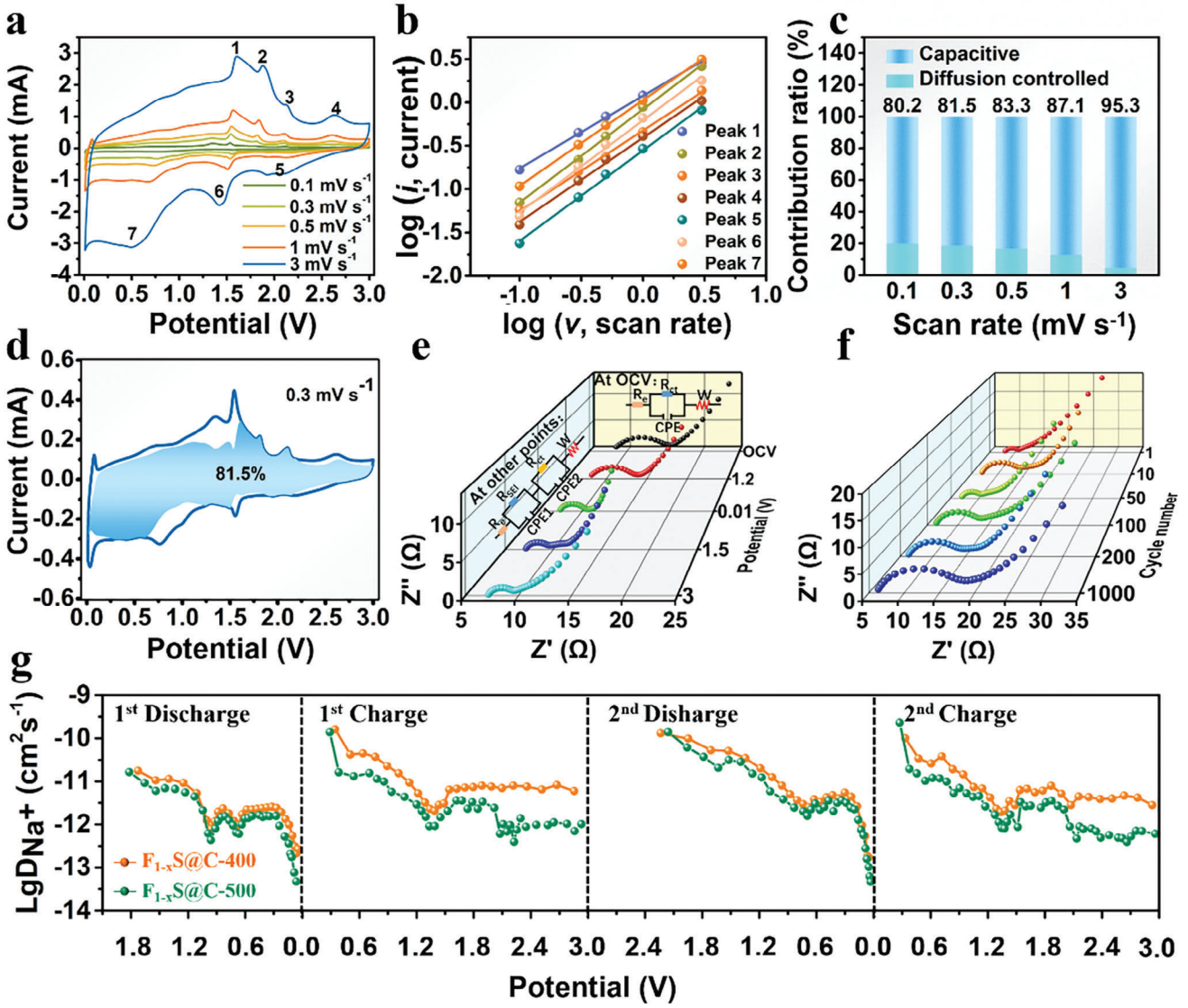

Figure 5. Kinetics investigation of the as-synthesized $Fe_{1-x}S$@C-400 composite. a) CV curves at various scan rates ranging from 0.1 to 3 mV s^{-1}. b) corresponding log i versus log v plots at each redox peak (peak current: i, scan rate: v). c) bar chart exhibiting the contribution ratio of pseudocapacitive contribution at various scan rates. d) CV curve with the pseudocapacitive contribution shown by the cyan region at a scan rate of 0.3 mV s^{-1}; e) First charge/discharge profile at 0.5 A g^{-1} with labeled points for in situ EIS; f) EIS spectra after different cycles; g) Na ion diffusion coefficients of the first two cycles at different discharge and charge state of $Fe_{1-x}S$@C composites.

nanoparticles, which are ≈5 nm or less, making them comparable to or even smaller than the diffusion distance of iron during cation exchange. As a result, these nanoparticles can offer thermodynamically reversible nanodomains for the conversion reaction of metallic Fe and Na_2S.[18] This finding demonstrates that the sluggish reaction kinetics of sulfur and Na_2S can be effectively improved by ultrafine pulverization, leading to a significant enhancement in specific capacity and cycling stability. The electrochemical reaction mechanism is summarized in Figure 4e. Furthermore, the graphitization degree of the $Fe_{1-x}S$@C-400 composite was also investigated by ex situ Raman during the initial cycle. Figure S11 (Supporting Information), exhibited the graphitization degree of carbon materials (I_D/I_G) in $Fe_{1-x}S$@C-400 composite continues to decrease as the cycle proceeds, indicating abundant defects, vacancies, and a higher degree of disorder. It should be pointed out that the highly disordered structure would be more beneficial to offer extra active sites for large sodium ions storage.[48]

To understand the excellent rate capability of $Fe_{1-x}S$@C-400 anode in SIBs, the kinetics of $Fe_{1-x}S$@C-400 anode was investigated by quantitatively studying the surface-controlled (capacitive) and diffusion-controlled charge storage contributions.[49] **Figure** 5a showed the CV response at various sweep rates from 0.1 to 3 mV s^{-1}. The current intensity increased with increasing sweep rate, and the CV curves kept the original shape and became a bit broader at a high scan rate of 3 mV s^{-1}. The electrochemical reactions occurred on the $Fe_{1-x}S$@C-400

electrode involving the diffusion-controlled or the surface-controlled
pseudocapacitive processes, which could be determined by the following equation:[50]

$$\log(i) = b\log(v) + \log(a) \quad (6)$$

where a and b are two adjustable parameters. When the value of b is close to 0.5, represents an ionic diffusion-controlled process, and when it gets close to 1.0, indicating a surface-controlled pseudo-capacitance mechanism. Several cathodic/anodic peaks were chosen (labeled as Peak1, 2, 3, 4, 5, 6, and 7) to evaluate the relationship between logarithmic current *i*) and scan rate *v*). According to the linear relationships between log *i*) and log *v*) as shown in Figure 5b, the obtained b values (slopes) of peaks 1, 2, 3, 4, 5, 6, and 7 were 0.83, 1.07, 0.92, 0.96, 1.04, 1.05, and 0.98, respectively, suggesting a pseudocapacitive-dominated behavior, and thus leading to excellent rate performance. The pseudocapacitive contribution was further calculated using the following equation:[51]

$$i(V) = k1v + k2v1/2 \quad (7)$$

where i(V) is the current at a fixed potential, k_1 and k_2 are adjustable parameters, k_1v and $k_2v^{1/2}$ are pseudocapacitive and diffusion-controlled contributions, respectively. Thus, by determining k_1 and k_2 constants, the pseudocapacitive contributions at different sweep rates can be calculated. As depicted in Figure 5c, along with increasing of sweep rate, it further increased and reached 95.3% at the sweep rate of 2 mV s^{-1} whilst the diffusion contribution gradually decreased. CV curves and corresponding capacitive proportion (ca. 81.5%, shaded area) at a sweep rate of 0.3 mV s^{-1} are depicted in Figure 5d, and the rest of the capacity contribution profiles at other scan rates were displayed in Figure S12 (Supporting Information). As a consequence, the surface-controlled pseudocapacitive contribution was dominant in the whole charge storage process, especially at high sweep rates.[52,53]

In situ electrochemical impedance spectroscopy (In situ EIS) during the initial discharge–charge cycle was carried out to study the electrochemical reaction kinetics differences induced by pulverization and phase transition of active materials at different sodiation-desodiation stages. Figure 5e exhibits the EIS spectra of the $Fe_{1-x}S$@C-400 electrode in the first discharge–charge cycle at various states. The Nyquist plots were composed of at least one depressed semicircle in the high- and middle-frequency range and an inclined line at low frequency, which agreed with the previous report. At the open-circuit voltage (OCV) state, the semicircle in the high-frequency region was related to the charge-transfer resistance (Rct), which resulted from the poor electrical conductivity of the active materials, and the inclined line in the low-frequency region was ascribed to the Warburg impedance (W) associated with the diffusion coefficient of Na^+ at the interface between the electrode and the electrolyte.[54] However, at other states, the semicircle corresponded to the mutual effect of SEI film resistance (R_{SEI}) and Rct.[55] In general, the resistance increased obviously from OCV to 0.01 V because of the formation of a nonconductive sodium sulfide matrix and SEI films and volume change.[56] However, an unexpected decreasing resistance phenomenon was observed during the discharge cycle, which could be ascribed to the pulverization of $Fe_{1-x}S$@C-400 with more exposed metallic Fe^0. During the charge cycle, the $Na_yFe_{1-x}S$ and $Fe_{1-x}S$ phase gradually increased and insulative sodium sulfide gradually decreased. Thereby, the resistance decreased gradually from 0.01 to 3.0 V. In addition, EIS tests were also measured after various cycles at a current density of 20 A g^{-1} to show the charge-transfer stability. With the increasing number of cycles, the resistance of the $Fe_{1-x}S$ electrode gradually increased (Figure 5f).

Moreover, the Galvanostatic intermittent titration technique (GITT) was further carried out to study the influence of multistep sodiation and desodiation reactions of $Fe_{1-x}S$@C-400 composite on sodium-ion diffusion coefficient. The ion diffusivity D_{Na} can be obtained by following the formula:[57]

$$DNa = \frac{4}{\pi\Delta\tau}\left(\frac{m_B V_M}{M_B S}\right)\left(\frac{\Delta E_S}{\Delta E_\tau}\right)^2 \quad (8)$$

Where τ, m_B, V_M, M_B, S, ΔE_s, and ΔE_τ represent the duration of the current impulse, the mass load of the electrode material, the molar volume of the materials, molar weight, geometric area of the electrode, quasi-thermodynamic equilibrium potential difference between before and after the current pulse, and voltage change caused by pulse, respectively. Figure S13 (Supporting Information) showes a typically amplified titration, different parameters (ΔE_s, and ΔE_τ, etc.), and the well-fitted line among the voltage (V) and duration time (t) in this single process. Note that E_o induced by the current pulse was not counted in ΔE_τ for discharge and charge GITT. Considering the pulverization process occurred in the initial cycle, the first two discharge/charge processes were recorded, as shown in Figure S14a (Supporting Information). The Na-ion diffusion coefficients of the $Fe_{1-x}S$@C-400 anode at different discharge and charge states were calculated and plotted in Figure 5g and compared with those of the $Fe_{1-x}S$@C-500 anode. The corresponding sodium diffusion coefficients of $Fe_{1-x}S$@C-400 were higher than those of $Fe_{1-x}S$@C-500. This was mainly attributed to the ultrafine pulverization of $Fe_{1-x}S$@C-400 composite, which has a higher ionic conductivity compared with $Fe_{1-x}S$@C-500. The D_{Na} varying tendencies of the first two cycles were similar during the sodiation and desodiation, and the Na-ion diffusion coefficient of the $Fe_{1-x}S$@C-400 electrode has a value between 1.71×10^{-13} and 1.60×10^{-10} cm^2 s^{-1}. Note that the minimum values at the total discharge state represent the deep diffusion of Na^+ ions in the anode. It was reasonable to assume that the surface of carbon was easier to capture Na-ion than the inner part. As the surface-active sites were gradually occupied, Na-ion began to insert into the carbon. However, the Na-ion had to overcome the repulsion force from the adsorbed Na-ion that could lead to a remarkable reduction in D_{Na}. With the insertion length increasing, the D_{Na} gradually becomes lower and lower.[49] Accordingly, it exhibited high D_{Na} values at the starting charge process, and then gradually reduced. The average D_{Na} values of $Fe_{1-x}S$@C-400 at the first discharge and charge plateaus were $\approx 2.29 \times 10^{-12}$ and 6.93×10^{-12} cm^2 s^{-1}, respectively. The average D_{Na} values at the second discharge and charge plateaus were $\approx 5.01 \times 10^{-12}$ and 4.98×10^{-12} cm^2 s^{-1}, respectively. While the average D_{Na} values at the first and second charge processes shared similar values at each state, indicating the pulverization process mainly occurred during the initial discharge process and

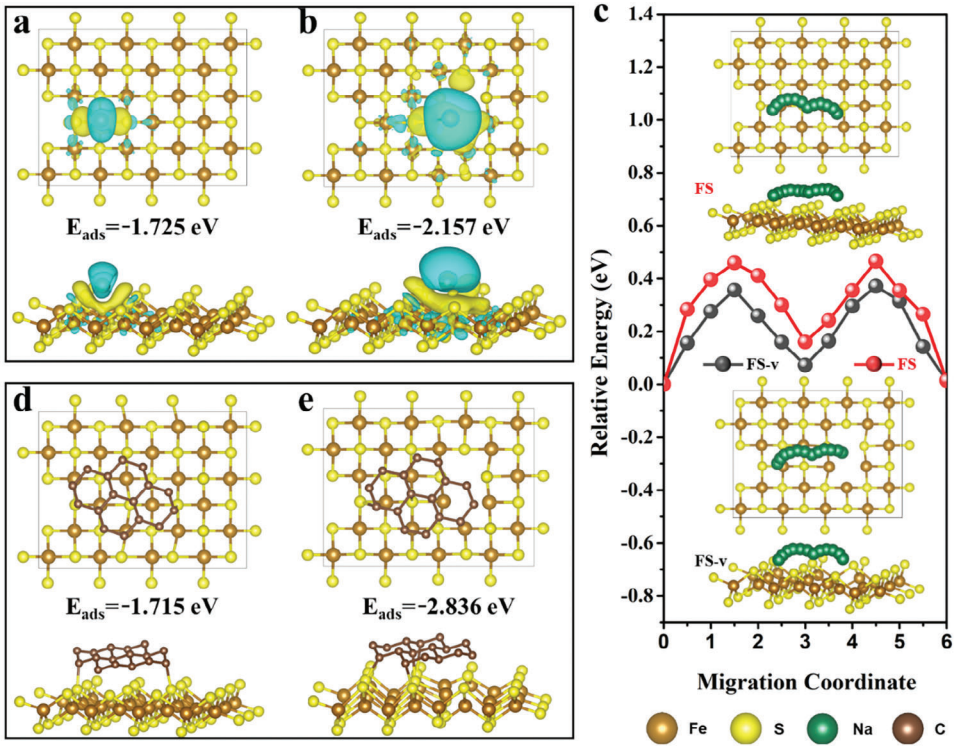

Figure 6. Top view and side view of the charge density differences and the corresponding adsorbed energies with one Na atom adsorbed on a) FS surface and b) FS-v surface, greenish yellow, and cyan areas represent the charge accumulation and loss, respectively; c) Na-ion migration path (top view and side view) and diffusion energy barriers on FS and FS-v surface; Top view, side view, and the corresponding adsorbed energies of the optimized geometries for the interaction and bonding between carbon and $Fe_{1-x}S$: d) carbon with FS surface and e) carbon with FS-v surface.

the stability of the electrode after pulverization. Furthermore, the third cycle GITT curve was also recorded to compare with the initial two cycles, and the Na-ion diffusion coefficients at the third discharge and charge states were calculated and plotted in Figure S14b (Supporting Information). It can be seen that the average D_{Na} values at the third discharge–charge processes achieved comparable values at each state with that of the second discharge–charge processes, which further implied the superior stability of the $Fe_{1-x}S$@C anode after the initial cycle.

DFT calculations were conducted to get further insight into the impressive electrochemical performance of the $Fe_{1-x}S$@C-400 anode. Here, we considered that the initial state of $Fe_{1-x}S$ nanoparticles (denoted as FS) is defect-free, while the nanocrystal is defective after the pulverization (denoted as FS-v), and both crystal models were constructed and displayed in Figure S15 (Supporting Information). First, the adsorption energies (E_{ads}) between Na ion and the surface of FS and FS-v were calculated. Figure S16 (Supporting Information) displayed the Na adsorbed on the surface of FS and FS-v (top view and side view). **Figure** 6a,b presents the 3D charge density differences of single Na atom adsorbed on the surface FS and FS-v, respectively, where the electron-rich and hole-rich regions are distributing obviously, and the charge accumulation (greenish-yellow parts) and charge depletion (cyan parts) revealed the charge transfer from Na^+ to FS and FS-v. For Na/FS-v system, the charge accumulation was observed not only between the Na atom and FS-v interface but also between the Na atom and vacancies. The FS-v surface possessed a larger amount of charge accumulation than that of the FS surface, indicating a stronger binding energy between Na^+ and FS-v. This result was further confirmed through the adsorption energy calculation. The E_{ads} values of a single Na ion on FS and FS-v surface were −1.725 and −2.157 eV, respectively. It demonstrated that the existence of vacancies could enhance the Na^+ adsorption ability of $Fe_{1-x}S$. Second, the migration energy barrier was also calculated to evaluate the Na-ion transport. Figure 6c displays the Na ion diffusion path and energy barriers on both surfaces of FS and FS-v. It was obvious that the energy barriers for FS-v were lower than those for FS, manifesting that the defects could facilitate the Na-ion diffusion kinetics. Finally, the adsorption energies between nanoparticles (FS and FS-v) and carbon substrate were also calculated to further understand the non-aggregation phenomenon after the pulverization process. In general, nanosized particles tend to aggregate during the electrochemical sodiation/desodiation process, resulting in an inevitable capacity decay. Surprisingly, the aggregation phenomenon after this ultrafine pulverization process did not happen in subsequent cycling. It was speculated that the pulverized $Fe_{1-x}S$ nanoparticles attached to or embedded in a carbon matrix and thus avoided the aggregation. To get a deep understanding of the above phenomenon, the surface chemical bond between carbon and FS-v nanoparticles was further investigated by DFT calculation. The adsorption energies (E_{ads}) calculated between carbon and the surface of FS and FS-v were −1.715 and −2.836 eV, respectively, exhibiting more negative adsorption

energy after pulverization (Figure 6d,e). Based on the experiment finding and theoretical calculation, it was speculated that the pulverized $Fe_{1-x}S$ ultrafine nanoparticles attached to or embedded in a carbon matrix and thus avoided aggregation, and the more negative adsorption energy between carbon and FeS-V was more beneficial to the fixation of ultrafine nanoparticles on the surface of carbon, thereby effectively avoiding aggregation during repeated discharge/charge process. Consequently, the $Fe_{1-x}S$@C simultaneously exhibited high reversible capacity, superior rate capability, and ultralong cycling stability.

3. Conclusion

In summary, ultrathin $Fe_{1-x}S$@C nanoplates have been prepared successfully via a facile coating-carbonation-sulfidation strategy. When used as an anode material for SIBs, an interesting ultrafine pulverization phenomenon of the $Fe_{1-x}S$@C anode during the first discharge was observed, and the $Fe_{1-x}S$@C nanoplates were completely pulverized into ultrafine particles with quantum size (≈ 5 nm) and no discernable aggregation was detected in subsequent cycles. In situ XRD and Raman demonstrated that the pulverized ultrafine particles can significantly overcome the kinetic and thermodynamic limitations of the conversion reaction, realizing the highly reversible conversion reaction of $Fe_{1-x}S$. Additionally, the kinetics analysis revealed that the capacity contribution was dominated by capacitive behavior. DFT calculations further deciphered that the pulverization of ultrathin carbon-coated $Fe_{1-x}S$ nanoplates could not only significantly reduce both the adsorbed energies and diffusion energy barriers of Na atom but also effectively prevent the aggregation of $Fe_{1-x}S$ particles by strengthening the adsorption between pulverized $Fe_{1-x}S$ nanoparticles and carbon. Benefiting from the unique ultrafine pulverization, the $Fe_{1-x}S$@C anode simultaneously exhibited high reversible capacity (610 mAh g^{-1} at 500 mA g^{-1}), and excellent rate capability (427.9 mAh g^{-1} at 20 A g^{-1}), and long-term cycle stability (377.9 mAh g^{-1} after 2500 cycles at 20 A g^{-1}). This work holds a meaningful insight into the nanomaterial engineering strategies and pulverization phenomenon and might suggest a possible way to design advanced electrode materials for energy storage devices.

Supporting Information

Supporting Information is available from the Wiley Online Library or from the author.

Acknowledgements

This work was supported by the National Science Fund for Distinguished Young Scholars (51625102), the National Natural Science Foundation of China (51971065), and the Innovation Program of Shanghai Municipal Education Commission (2019-01-07-00-07-E00028). The authors would like to thank SCI-GO (www.sci-go.com) for the TEM analysis.

Conflict of Interest

The authors declare no conflict of interest.

Data Availability Statement

The data that support the findings of this study are available in the supplementary material of this article.

Keywords

$Fe_{1-x}S$@C, pulverization, quantum size, reversible conversion reactions, sodium-ion batteries

Received: December 27, 2023
Revised: February 29, 2024
Published online:

[1] J.-Y. Hwang, S.-T. Myung, Y.-K. Sun, *Chem. Soc. Rev.* **2017**, *46*, 3529.
[2] T. Rojo, Y. S. Hu, M. Forsyth, X. Li, *Handb. Sodium-Ion Batteries* **2018**, *8*, 1800880.
[3] J. Peters, D. Buchholz, S. Passerini, M. Weil, *Energy Environ. Sci.* **2016**, *9*, 1744.
[4] P. Geng, S. Zheng, H. Tang, R. Zhu, L. Zhang, S. Cao, H. Xue, H. Pang, *Adv. Energy Mater.* **2018**, *8*, 1703259.
[5] L. Li, S. Peng, N. Bucher, H.-Y. Chen, N. Shen, A. Nagasubramanian, E. Eldho, S. Hartung, S. Ramakrishna, M. Srinivasan, *Nano Energy* **2017**, *37*, 81.
[6] Y. Chen, X. Hu, B. Evanko, X. Sun, X. Li, T. Hou, S. Cai, C. Zheng, W. Hu, G. D. Stucky, *Nano Energy* **2018**, *46*, 117.
[7] Z. Man, P. Li, D. Zhou, Y. Wang, X. Liang, R. Zang, P. Li, Y. Zuo, Y. M. Lam, G. Wang, *Nano Lett.* **2020**, *20*, 3769.
[8] L. David, R. Bhandavat, G. Singh, *ACS Nano* **2014**, *8*, 1759.
[9] Z. Hu, L. Wang, K. Zhang, J. Wang, F. Cheng, Z. Tao, J. Chen, *Angew. Chem., Int. Ed.* **2014**, *53*, 12794.
[10] X. Song, X. Li, Z. Bai, B. Yan, D. Li, X. Sun, *Nano Energy* **2016**, *26*, 533.
[11] W. Shuang, H. Huang, L. Kong, M. Zhong, A. Li, D. Wang, Y. Xu, X.-H. Bu, *Nano Energy* **2019**, *62*, 154.
[12] F. Xie, L. Zhang, Q. Gu, D. Chao, M. Jaroniec, S.-Z. Qiao, *Nano Energy* **2019**, *60*, 591.
[13] J. Lin, L. Yao, C. Zhang, H. Ding, Y., Wu, S. Li, J. Han, G. Yue, D. Peng, *ACS Sustainable Chem. Eng.* **2021**, *9*, 11280.
[14] H. Gao, T. Zhou, Y. Zheng, Q. Zhang, Y. Liu, J. Chen, H. Liu, Z. Guo, *Adv. Funct. Mater.* **2017**, *27*, 1702634.
[15] L. Zhou, K. Zhang, J. Sheng, Q. An, Z. Tao, Y.-M. Kang, J. Chen, L. Mai, *Nano Energy* **2017**, *35*, 281.
[16] M. Ma, Y. Yao, Y. Wu, Y. Yu, *Adv. Fiber Mater.* **2020**, *2*, 314.
[17] L. L. Li, S. J. Peng, N. Bucher, H. Y. Chen, N. Shen, A. Nagasubramanian, E. Eldho, S. Hartung, S. Ramakrishna, M. Srinivasan, *Nano Energy* **2017**, *37*, 81.
[18] A. Douglas, R. Carter, L. Oakes, K. Share, A. P. Cohn, C. L. Pint, *ACS Nano* **2015**, *9*, 11156.
[19] Y. Zhao, J. Zhu, S. J. H. Ong, Q. Yao, X. Shi, K. Hou, Z. J. Xu, L. Guan, *Adv. Energy Mater.* **2018**, *8*, 1802565.
[20] Z. Hu, Z. Zhu, F. Cheng, K. Zhang, J. Wang, C. Chen, J. Chen, *Energy Environ. Sci.* **2015**, *8*, 1309.
[21] S. G. Zhang, J. Mi, H. P. Zhao, W. Y. Ma, L. Y. Dang, L. C. Yue, *J. Alloys Compd.* **2020**, *842*, 155642.
[22] Y. Wu, L. Wu, S. Wu, Y. Yao, Y. Feng, Y. Yu, *Small Sci.* **2021**, *1*, 2100059.
[23] Z. Yan, Y. Liang, J. Xiao, W. Lai, W. Wang, Q. Xia, Y. Wang, Q. Gu, H. Lu, S. L. Chou, *Adv. Mater.* **2020**, *32*, 1906700.
[24] Q. Pan, Z. Tong, Y. Su, S. Qin, Y. Tang, *Adv. Funct. Mater.* **2021**, *31*, 2103912.
[25] Z. Liu, T. Lu, T. Song, X.-Y. Yu, X. W. D. Lou, U. Paik, *Energy Environ. Sci.* **2017**, *10*, 1576.

[26] M. J. Choi, J. Kim, J. K. Yoo, S. Yim, J. Jeon, Y. S. Jung, *Small* **2018**, *14*, 1702816.
[27] Q. Li, Q. Wei, W. Zuo, L. Huang, W. Luo, Q. An, V. O. Pelenovich, L. Mai, Q. Zhang, *Chem. Sci.* **2017**, *8*, 160.
[28] Q. Ma, H. Song, Q. Zhuang, J. Liu, Z. Zhang, C. Mao, H. Peng, G. Li, K. Chen, *Chem. Eng. J.* **2018**, *338*, 726.
[29] X. Li, H. Wang, W. Zhang, Y. Feng, J. Ma, *Acta Metall. Sin.* **2021**, *34*, 321.
[30] Q. Yuan, Y. Chen, A. Li, Y. Li, X. Chen, M. Jia, H. Song, *Appl. Surf. Sci.* **2020**, *508*, 145286.
[31] A. Ramadoss, S. J. Kim, *Carbon* **2013**, *63*, 434.
[32] Y. Liu, Y. Fang, Z. Zhao, C. Yuan, X. W. Lou, *Adv. Energy Mater.* **2019**, *9*, 1803052.
[33] H. Fan, B. Qin, Z. Wang, H. Li, J. Guo, X. Wu, J. Zhang, *Sci. China Mater.* **2020**, *63*, 505.
[34] Q. L. Wei, Y. Q. Fu, G. X. Zhang, Y. L. Wang, X. Y. Wang, M. Mohamedi, S. H. Sun, *RSC Adv.* **2016**, *6*, 84149.
[35] F. H. Yang, Z. A. Zhang, K. Du, X. X. Zhao, W. Chen, Y. Q. Lai, J. Li, *Carbon* **2015**, *91*, 88.
[36] Q. Pan, F. Zheng, X. Ou, C. Yang, X. Xiong, Z. Tang, L. Zhao, M. J. A. S. C. Liu, *ACS Sustainable Chem. Eng.* **2017**, *5*, 4739.
[37] Q. Pan, F. Zheng, Y. Liu, Y. Li, W. Zhong, G. Chen, J. Hu, C. Yang, M. Liu, *J. Mater. Chem. A* **2019**, *7*, 20229.
[38] Y. X. Wang, J. Yang, S. L. Chou, H. K. Liu, W. X. Zhang, D. Zhao, S. X. Dou, *Nat. Commun.* **2015**, *6*, 8689.
[39] L. Cao, X. W. Gao, B. Zhang, X. Ou, J. F. Zhang, W. B. Luo, *ACS Nano* **2020**, *14*, 3610.
[40] Y. Xu, Y. Wen, Y. Zhu, K. Gaskell, K. A. Cychosz, B. Eichhorn, K. Xu, C. Wang, *Adv. Funct. Mater.* **2015**, *25*, 4312.
[41] Z. Lu, J. R. Dahn, *J. Electrochem. Soc.* **2001**, *148*, A1225.
[42] G. K. Veerasubramani, Y. Subramanian, M. S. Park, G. Nagaraju, B. Senthilkumar, Y. S. Lee, D. W. Kim, *J. Mater. Chem. A* **2018**, *6*, 20056.
[43] K. Zhang, M. Park, L. Zhou, G. H. Lee, J. Shin, Z. Hu, S. L. Chou, J. Chen, Y. M. Kang, *Angew. Chem., Int. Ed.* **2016**, *55*, 12822.
[44] H. Wan, J. P. Mwizerwa, X. Qi, X. Xu, H. Li, Q. Zhang, L. Cai, Y.-S. Hu, X. Yao, *ACS Appl. Mater. Interfaces* **2018**, *10*, 12300.
[45] Y. Xu, F. Bahmani, R. Z. Wei, *Microsyst. Nanoeng.* **2020**, *6*, 75.
[46] I. Weber, U. Böttger, S. Pavlov, H. W. Hübers, H. Hiesinger, E. K. Jessberger, *J. Raman Spectrosc.* **2017**, *48*, 1509.
[47] L. Almanqur, I. Vitorica-Yrezabal, G. Whitehead, D. J. Lewis, P. O'Brien, *RSC Adv.* **2018**, *8*, 29096.
[48] P. Lu, Y. Sun, H. Xiang, X. Liang, Y. Yu, *Adv. Energy Mater.* **2018**, *8*, 1702434.
[49] D. Chao, C. Zhu, P. Yang, X. Xia, J. Liu, J. Wang, X. Fan, S. V. Savilov, J. Lin, H. J. Fan, *Nat. Commun.* **2016**, *7*, 12122.
[50] C. S. An, Y. F. Yuan, B. Zhang, L. B. Tang, B. Xiao, Z. J. He, J. C. Zheng, J. Lu, *Adv. Energy Mater.* **2019**, *9*, 1900356.
[51] Y. Gogotsi, R. M. J. A. Penner, *ACS Nano* **2018**, *12*, 2081.
[52] C. X. Huang, Y. H. Ding, C. Hao, S. S. Zhou, X. H. Wang, H. W. Gao, L. L. Zhu, J. B. Wu, *Chem. Eng. J.* **2019**, *378*, 122202.
[53] J. Y. Go, S. I. Pyun, *J. Solid State Electrochem.* **2007**, *11*, 323.
[54] W. Choi, H. C. Shin, J. M. Kim, J. Y. Choi, W. S. Yoon, *J. Electrochem. Sci. Technol.* **2020**, *11*, 1.
[55] H. Y. Lu, L. Wu, L. F. Xiao, X. P. Ai, H. X. Yang, Y. L. Cao, *Electrochim. Acta* **2016**, *190*, 402.
[56] S. H. Dong, C. X. Li, Z. Q. Li, L. Y. Zhang, L. W. Yin, *Small* **2018**, *14*, 1704517.
[57] F. Feng, S. L. Chen, S. Q. Zhao, W. L. Zhang, Y. G. Miao, H. Y. Che, X. Z. Liao, Z. F. Ma, *Chem. Eng. J.* **2021**, *411*, 128518.